ELSEVIER

Contents lists available at ScienceDirect

International Journal of Greenhouse Gas Control

journal homepage: www.elsevier.com/locate/ijggc



Time-lapse pressure tomography for characterizing CO₂ plume evolution in a deep saline aquifer



Linwei Hu^{a,*}, Peter Bayer^a, Peter Alt-Epping^b, Alexandru Tatomir^c, Martin Sauter^c, Ralf Brauchler^d

- ^a ETH Zurich, Department of Earth Sciences, Sonneggstrasse 5, 8092 Zurich, Switzerland
- ^b University of Bern, Institute of Geological Sciences, Baltzerstrasse 3, 3012 Bern, Switzerland
- ^c University of Göttingen, Geoscience Center, Goldschmidtstrasse 3, 37077 Göttingen, Germany
- ^d AF-Consult Switzerland Ltd, Täfernstrasse 26, 5405 Baden, Switzerland

ARTICLE INFO

Article history: Received 5 November 2014 Received in revised form 20 March 2015 Accepted 22 April 2015

Keywords: Two-phase flow in porous media Mixed-phase flow Deep saline aquifer Pressure tomography CO₂ plume monitoring

ABSTRACT

A time-lapse pressure tomography inversion approach is applied to characterize the CO2 plume development in a virtual deep saline aquifer. Deep CO₂ injection leads to flow properties of the mixed-phase, which vary depending on the CO₂ saturation. Analogous to the crossed ray paths of a seismic tomographic experiment, pressure tomography creates streamline patterns by injecting brine prior to CO2 injection or by injecting small amounts of CO2 into the two-phase (brine and CO2) system at different depths. In a first step, the introduced pressure responses at observation locations are utilized for a computationally rapid and efficient eikonal equation based inversion to reconstruct the heterogeneity of the subsurface with diffusivity (D) tomograms. Information about the plume shape can be derived by comparing Dtomograms of the aquifer at different times. In a second step, the aquifer is subdivided into two zones of constant values of hydraulic conductivity (K) and specific storage (S_s) through a clustering approach. For the CO_2 plume, mixed-phase K and S_s values are estimated by minimizing the difference between calculated and "true" pressure responses using a single-phase flow simulator to reduce the computing complexity. Finally, the estimated flow property is converted to gas saturation by a single-phase proxy, which represents an integrated value of the plume. This novel approach is tested first with a doublet well configuration, and it reveals a great potential of pressure tomography based concepts for characterizing and monitoring deep aquifers, as well as the evolution of a CO₂ plume. Still, field-testing will be required for better assessing the applicability of this approach.

© 2015 Elsevier Ltd. All rights reserved.

1. Introduction

Despite the rising awareness of global environmental changes and increased efforts in establishing renewable energy sources, global carbon dioxide (CO_2) emissions are still on a rise. Therefore, in the low-carbon energy strategies of many countries, carbon capture and storage (CCS) plays a prominent role. Instead of releasing CO_2 to the atmosphere, CCS implies the capturing CO_2 at the site of large producers and the storage in deep geological formations, mainly saline aquifers. Even though numerous test sites have been developed, only in a few cases large, industrial-scale amounts of CO_2 are injected into the subsurface, for instance, in former oil or gas reservoirs. Much attention has been paid to injecting

CO₂ into deep saline aquifers. These aquifers potentially offer enormous storage capacities (Bachu and Adams, 2003). However, large-scale applications are still scarce and thus long-term experience is missing. Injection of CO₂ into the subsurface involves many unknowns. Perhaps the most critical among these is the uncontrolled migration of CO₂. The injection of CO₂ in deep saline aquifer generates a plume, which may leak into overlying strata along existing geological fault/fractures or along abandoned wells or leaky well completion (Lemieux, 2011). Moreover, possible hydro-fracture propagation during long-term pressure evolution can create new leakage pathways. This underlines the importance of monitoring CO₂ plume behavior during and after short- and long-term injection periods.

Common approaches to characterize CO₂ plumes are based on established geophysical techniques, such as seismic surveys (e.g., Ajo-Franklin et al., 2013), electrical resistivity/conductivity surveys (e.g., Bergmann et al., 2012), and gravity monitoring (e.g.,

^{*} Corresponding author. Tel.: +41 44 633 83 12; fax: +41 44 633 11 08. E-mail address: linwei.hu@erdw.ethz.ch (L. Hu).

Nomenclature Α Tomographical matrix CO₂ compressibility (1/Pa) c_n Water compressibility (1/Pa) c_w c_r Heat capacity (J/kg) D Diffusivity (m²/s) \tilde{D}_n Diffusion coefficient of CO₂ in brine (m²/s) d Aguifer thickness (m) Conversion factor (–) $f_{\alpha,d}$ Gravity acceleration (m/s²) g Н Enthalpy (J/K) h Head (m) First time-derivative of head (m/s) $h_d(r,t)$ $h_d(r,t_{\text{peak}})$ Maximum first time-derivative value of head data Component Κ Mixed-phase hydraulic conductivity (m/s) K_{w} Single-phase hydraulic conductivity (m/s) Intrinsic permeability (m²) k Relative permeability of non-wetting phase (–) k_{rn} Relative permeability of wetting phase (-) k_{rw} Μ Local reliability indicator (-) \tilde{P} Global pressure (Pa) P_0 Datum pressure (Pa) Capillary pressure (Pa) P_c P_d Entry pressure (Pa) P_{w} Pressure of wetting phase (Pa) P_n Pressure of non-wetting phase (Pa) Q Source/sink term of mass (mol/s) Q_h Source/sink term of heat (W) Mass injection rate of CO₂ (kg/s) Q_c Mass injection rate of water (kg/s) Q_w Volumetric injection rate of CO_2 (m³/s) q_n Volumetric injection rate of brine (m³/s) q_w Well radius (m) r_w Saturation of non-wetting phase (–) S_n Residual saturation of non-wetting phase (-) S_{nr} S_w Saturation of wetting phase (-) S_{wr} Residual saturation of wetting phase (-) S_s Mixed-phase specific storage (1/m) S_{sw} Single-phase specific storage (1/m) Propagation path (m) S T Temperature (K) T_0 Initial temperature (K) Early time diagnostic (s) $t_{\alpha,d}$ t_{peak} U Peak travel time (s) Internal energy (J) U Left singular vector V Right singular vector и Darcy flow velocity (m/s) W Lambert's W function W Diagonal matrix X_i^{α} Molar fraction (−) Injection point (m) χ_1 Observation point (m) χ_2 Greek symbols Phase index ($\alpha = w$: wetting phase; $\alpha = n$: non- α wetting phase) Thermal conductivity coefficient (W/mK) К Dry rock thermal conductivity (W/mK) κ_{dry} Wet rock thermal conductivity (W/mK) κ_{wet}

```
λ
           Pore size distribution (−)
\lambda_T
           Total mobility (1/Pas)
           Mobility of wetting phase (1/Pas)
\lambda_w
           Mobility of non-wetting phase (1/Pas)
\lambda_n
\mu_{w}
           Viscosity of wetting phase (Pas)
\mu_n
           Viscosity of non-wetting phase (Pas)
\widetilde{\rho}
           Molar density (mol/m<sup>3</sup>)
           Dynamic mixed-phase density (kg/m<sup>3</sup>)
\rho_d
           Mass density of non-wetting phase (kg/m^3)
\rho_n
\rho_r
           Rock density (kg/m<sup>3</sup>)
           Static mixed-phase density (kg/m<sup>3</sup>)
\rho_{s}
           Mass density of wetting phase (kg/m<sup>3</sup>)
\rho_{w}
           Tortuosity (−)
```

Chadwick et al., 2006). Additionally, distributed acoustic sensing is considered as an innovative means for CO_2 monitoring (e.g., Daley et al., 2013). All of these techniques represent indirect ways of characterizing the CO_2 plume and its migration. None of these offers a direct relationship between CO_2 saturation and the hydraulic regime in the deep aquifer. For instance, in seismic surveys the relationship between seismic waves and CO_2 saturation is site-specific, non-linear, and associated with a high signal-to-noise ratio. Moreover, for seismic tomography and electrical resistance tomography (ERT), the coarse spatial resolution may be a limiting factor, given that residual CO_2 often forms meter–scale plumes (Martinez-Landa et al., 2013).

Apart from geophysical approaches, fluid injection/extraction tests (water, CO₂ or water-CO₂ mixture) can be used to derive two-phase flow properties. Two-phase flow properties are different from single-phase flow properties because injected CO₂ will introduce a high compressibility to the flow system (Vilarrasa et al., 2010). Further, the total mobility (summation of the separate phase mobility) of the phase mixture (CO₂, water or brine) in the aquifer varies due to the lower viscosity of the CO₂ phase. All these effects directly influence the pressure responses from fluid injection tests.

Previous studies have shown that both single-phase and twophase flow properties can be derived from fluid injection/extraction tests by pressure data analysis. Interference pumping tests prior to CO₂ injection were proposed by Doughty et al. (2004) for characterizing the single-phase flow properties of the potential storage formation. Wiese et al. (2010) pointed out that pressure data obtained from single-well and cross-well pumping tests conducted before CO₂ injection can be used to identify the hydraulic connectivity and the boundary type of the formation at the Ketzin site, Germany. The pressure evolution during CO₂ injection can also be used for estimating flow properties. When CO₂ is injected in small amounts, pressure data from the injection well and a monitoring well can be used to constrain the permeability of the formation (Sminchak et al., 2009). Doughty et al. (2008) estimated residual brine and CO2 saturations from transient pressure data derived from a CO₂ injection test at Frio Brine Pilot, Texas, United States. Sun and Nicot (2012) developed a pressure anomaly inversion procedure for detecting CO₂ leakage locations and rates from abandoned wells. Martinez-Landa et al. (2013) proposed a single-well CO₂ saturated brine injection test in a brine-CO₂ system with a low injection rate to identify the residual CO₂ saturation and the width of the CO₂ plume near the well by pressure data analysis. Mishra et al. (2013) derived an analytical solution to track a CO₂ front by analyzing the transient pressure data at the observation well. However, none of these approaches can delineate the spatial extent of the CO₂ plume based on pressure data.

Detailed knowledge of aquifer properties necessary for tracking the CO₂ plume is typically hampered by the small number of

available exploration boreholes. Conventional injection/extraction tests can only provide integral information of natural or induced flow properties of an aquifer. Cross-well injection/extraction tests that work with well pairs can, to some extent, provide averaged flow parameters between wells (Wu et al., 2005). In the field of petroleum reservoir engineering, interference tests and pulse tests are commonly used to characterize the reservoir (e.g., Fokker et al., 2012), as well as to inspect two-phase properties (e.g., Finsterle and Pruess, 1996; Fokker and Verga, 2011). These tests, however, cannot delineate the spatial heterogeneity of the subsurface (Freyberg, 1986). Geostatistical interpolation can be applied to reconstruct flow properties of the subsurface based on the data from a dense borehole network. However, because boreholes penetrating into deep aquifers are scarce, borehole-based geostatistical data analysis cannot provide accurate information of medium properties for large-scale flow and transport problems (Illman et al., 2007).

During the last twenty years, hydraulic tomography evolved as an alternative to conventional hydraulic field testing, because it is specifically suited for reconstructing the spatial distribution of hydraulic aquifer parameters (e.g., Butler et al., 1999; Yeh and Liu, 2000; Bohling et al., 2002; Brauchler et al., 2007, 2011; Mao et al., 2013). This approach is based on a series of hydraulic tests with a single fluid, i.e., water. The method utilizes a series of induced pressure changes, which are used to reconstruct spatial heterogeneity of single-phase flow properties by an inversion scheme. In analogy to seismic tomography, a series of space-filling streamline patterns can be generated by a combination of several different injection intervals (source) and observation points (receiver) (Butler et al., 1999). With sufficiently recorded data, an appropriate inverse model can then be used to obtain a reliable image of the subsurface.

One variant of hydraulic tomographical inversion is based on the approximation of the transient groundwater flow equation by an eikonal equation (Virieux et al., 1994). Ray tracing or particle tracking techniques are commonly applied to solve the eikonal equation by the calculation of pressure propagation paths (e.g., Vasco et al., 2000; Kulkarni et al., 2001; Brauchler et al., 2003, 2010). A core element in hydraulic tomography is that hydraulic diffusivity (i.e., the ratio of hydraulic conductivity and specific storage) is directly related to measured travel times of pressure perturbation. In analogy to seismic travel time inversion, spatial distribution of hydraulic diffusivity thus can be obtained in a computationally rapid and efficient way. However, the inverted diffusivity tomogram can only serve as a proxy mapping of the true diffusivity structure of the aquifer. Also specific values of the hydraulic conductivity and the specific storage cannot be derived from inverted tomograms. Hence, the reconstructed structure is usually employed as the starting model for a second inversion step based on full signal calibration with a forward groundwater flow model (Hu et al., 2011; Jiménez et al., 2013).

Similar to the travel-time based hydraulic tomography approach in shallow aquifers, pressure tomography can be used to identify, characterize and monitor the spatial extent of the CO₂ plume. The underlying idea is that through injection, a mixed brine-CO₂ phase forms in the deep aquifer, which induces an apparent transient heterogeneity in the hydraulic properties of the system. Short-term fluid or gas injection in combination with a tomographical set-up can facilitate a rapid and efficient travel-time based inversion. This will provide qualitative aguifer diffusivity maps that can be utilized for tracking the migrating CO₂ plume. However, quantitative estimates of the spatial distribution of CO₂ saturation are only possible by calibration with an appropriate multi-phase forward model. Also, in comparison to hydraulic tomography in shallow aquifers, practical limitations will be the costs for drilling and instrumentation of multiple deep boreholes, which are needed for obtaining a spatial resolution.

The main objective of this paper is to develop a fundamentally new pressure-based tomographical approach to delineate the CO_2 plume. In contrast to other geophysical methods this approach has potential to directly compute spatially averaged CO_2 saturations by the two-phase flow properties. In the following, we shortly describe the travel-time based procedure for deriving diffusivity tomograms. The structural information from these tomograms is extracted by zonal clustering, which in a homogeneous aquifer can be used to determine the shape of the plume. We then discuss ways of how to simplify computationally demanding multi-phase flow models. We propose a streamlined single-phase model, which emulates the multi-phase system, while substantially speeding up the ultimate calibration of the forward model. As an example for a real case application, we choose a two-dimensional simplified virtual site to develop our approach.

2. Methodology

2.1. Overview: cross well testing and inversion

For the injection model used in this study it is assumed that CO₂ is injected through a source well in a deep aquifer, and pressure changes are monitored in one nearby observation well that acts as a receiver. These pressure changes originate from injection at different depths at the source and are recorded at different levels along the observation well screen. A packer system allows partitioning of the injection interval at the source well. This facilitates a high-resolution tomographic analysis of multiple source-receiver combinations. The pressure pulses may be introduced by water or brine injection ahead of the CO₂ injection in order to characterize the pre-injection hydraulic conditions in the aguifer. Alternatively, it is also possible to use depth-dependent short-term injection of CO₂ at the source intermittently to the sequestration procedure. Regardless of the injected compound and operation stage, the same procedure of pressure tomography will be applied for characterizing the reservoir.

By comparing the tomograms from different points in time, the propagation of the CO_2 plume can be recorded. In a first step, the inversion procedure of this time-lapse pressure-based tomography utilizes a common travel-time based hydraulic tomographical approach for structural imaging. Travel times can then be used to gain first order insights into the aquifer structure and structural changes. In a second step, the structured aquifer models are calibrated to the full pressure-response curves (zonal calibration). For reducing simulation time and increasing computational efficiency, the complex multi-phase conditions in the aquifer are approximated by a novel single-phase based emulator.

2.2. Pressure-based tomographical inversion

Our travel time inversion approach to obtain hydraulic tomograms from cross-well pressure tests is based on the work by Vasco et al. (2000). With their approach, the groundwater flow equation is approximated by an eikonal equation, efficiently solved by ray tracing or particle tracking techniques. Consider a transient pressure curve, resulting from a Dirac signal generated at point x_1 (source), traveling along the propagation path s, and recorded at point s (observation). The relationship between hydraulic travel time and hydraulic diffusivity is expressed by a line integral:

$$\sqrt{t_{peak}(x_2)} = \frac{1}{\sqrt{6}} \int_{x_1}^{x_2} \frac{ds}{\sqrt{D(s)}}$$
 (1)

where t_{peak} is the peak travel time of the recorded pressure curve, and D is the hydraulic diffusivity.

For our experiments, Heaviside type sources (i.e., the continuous injection) are applied in order to obtain more pronounced and far-reaching pressure signals compared to those from a Dirac type source. To use the inversion scheme to the Heaviside type injection tests, the first time-derivative of the pressure readings is required (Vasco et al., 2000). As found in the hydraulic tomography study by Hu et al. (2011), as well as in our work shown below, the peak times are not distinct, which is indicated by small variation of the time-derivative at the peak. Hence, to improve resolution early travel time diagnostic ($t_{\alpha,d}$) is used for the inversion. In fact, higher conductive parts of the subsurface can be resolved better by early travel time than by peak time diagnostic (Cheng et al., 2009). Further, the early travel times can be more accurately obtained than the peak times, because the curve of the time-derivative of pressure has a much sharper slope before the peak time. The early travel time diagnostic is computed by introducing a conversion factor $f_{\alpha,d}$ (Brauchler et al., 2003):

$$\sqrt{t_{\alpha,d}} = \frac{1}{\sqrt{6f_{\alpha,d}}} \int_{x_1}^{x_2} \frac{ds}{\sqrt{D(s)}}$$
 (2)

with

$$f_{\alpha,d} = -W\left(\frac{\alpha_d^{2/3}}{e}\right) \tag{3}$$

where W is Lambert's W function, and α_d corresponds to the hydraulic head ratio term defined as $\frac{h_d(r,t)}{h_d(r,t_{peak})}$, where $h_d(r,t_{peak})$ is the maximum value of the first time-derivative of pressure data for a Heaviside pulse. $h_d(r,t)$ is the first time-derivative of pressure as a function of time and space. In this study, we applied the 20% travel time diagnostic (t–20%, i.e., the time at which the pressure pulse rises to 20% of its ultimate peak value) for the inversion procedure (Hu et al., 2011). In our simulation study, wellbore storage is neglected. However, in practice, it can cause a delay of travel times (Prats and Scott, 1975). The influence of this delay decreases with distance between source and receiver. It can be estimated analytically and included in the travel time based inversion (Brauchler et al., 2007).

Following the travel-time based inversion, reliability of the inverted tomograms is evaluated by using the null space energy as indicator. For the concept of null space energy maps, we utilize the procedure proposed by Böhm and Vesnaver (1996). They estimated the ray distribution in pixels of a tomographical model to assess the stability of seismic velocity tomograms. A tomographical matrix **A** is decomposed into two orthonormal matrices (**U** and **V**) and a diagonal matrix **W** by singular value decomposition (SVD):

$$\mathbf{A} = \mathbf{U}\mathbf{W}\mathbf{V}^{\mathsf{T}} \tag{4}$$

where the elements of matrix $\bf A$ represent the total length of propagation paths in each pixel of the tomogram. The reliability of the inversion result can be assessed by the singular values, which are the elements of matrix $\bf W$. Small or zero values of the elements in matrix $\bf W$ indicate large instability in the solution of a tomographical system. However, the singular values can only be considered as a global indicator for reliability estimation. Each singular value relates to a column of the matrix $\bf V$, and it cannot provide detailed reliability at each pixel. Thus, a local reliability indicator, $\bf M$, is defined to describe the reliability of each pixel for the tomogram. The summation of the squared column element (v_i) of matrix $\bf V$ implies the orthonormal basis of the model domain:

$$M = \sum_{i} V_i^2 \tag{5}$$

The value of M ranks from 0 to 1. Here, we use M = 0.5 as the threshold to judge the reliability of inverted results. Inverted diffusivity

values with *M* smaller than 0.5 are considered as reliable, and if *M* is greater than 0.5, the values per pixel are considered as unreliable.

2.3. Clustering and zonal calibration

The inverted tomograms provide estimates of the cross-sectional diffusivity distribution at different times during sequestration, including pre-injection and post-injection conditions. To derive the plume distribution, the diffusivity data sets are partitioned into two clusters, one representing the plume and the other the ambient aquifer. k-means clustering is applied and two zones with constant conductivity and specific storage values are obtained. Through clustering and by comparison with the tomogram derived for the pre-injection stage, the plume can be identified at different operational times. Aside from this, the clusters can be used to constrain the spatial parameter distribution in a numerical flow model. Zones of equal hydraulic properties are determined by clustering of reliable diffusivity values in the inverted tomograms. The hydraulic properties are estimated by calibration to the pressure signals.

The saturation changes are assumed relatively small during a multilevel CO_2 injection test. This allows us to use a single-phase simulator ("emulator") that solves the pressure equation decoupled from the saturation equation. This emulator is then applied to calibrate the hydraulic properties of inverted zonal structure by minimizing the residuals between the observed and calculated pressure responses. For the zonal calibration, we use the parameter estimator PEST (Doherty, 2010). Ultimately, the calibrated specific storage will be used for calculating CO_2 saturations.

2.4. Forward modeling

The mass, energy conservation and moment equations of a two-phase two-component system are as follows (Lichtner, 1996; Helmig, 1997):

$$\frac{\partial}{\partial t} \left(\phi \sum_{\alpha} S_{\alpha} \widetilde{\rho}_{\alpha} X_{i}^{\alpha} \right) + \nabla \cdot \sum_{\alpha} \left(u_{\alpha} \widetilde{\rho}_{\alpha} X_{i}^{\alpha} - \phi \tau S_{\alpha} \widetilde{\rho}_{\alpha} \widetilde{D}_{\alpha} \nabla X_{i}^{\alpha} \right) \\
= Q_{i} \tag{6}$$

$$\frac{\partial}{\partial t} \left(\phi \sum_{\alpha} S_{\alpha} \rho_{\alpha} U_{\alpha} + (1 - \phi) \rho_{r} c_{r} T \right) + \nabla \cdot \left(\sum_{\alpha} u_{\alpha} \rho_{\alpha} H_{\alpha} - \kappa \nabla T \right)
= Q_{h}$$
(7)

$$u_{\alpha} = -\frac{kk_{r\alpha}}{\mu_{\alpha}} \left(\nabla P_{\alpha} - \rho_{\alpha} gz \right) \tag{8}$$

where ϕ is porosity, τ is tortuosity, S_{α} is phase saturation, $\widetilde{\rho}_{\alpha}$ is molar density of phase α , ρ_{α} is mass density of phase α , D_{α} is phase diffusivity coefficient, and X_i^{α} is molar fraction of component i (water or CO_2) in phase α (α = w, wetting phase; α = n, non-wetting phase). Parameter u_{α} is the Darcy velocity, Q_i and Q_h are source/sink terms of mass and heat, respectively, U_{α} is internal energy, H_{α} is enthalpy, ρ_r is rock density, κ is the thermal conductivity coefficient of the rock, c_r is the heat capacity of the rock, $k_{r\alpha}$ is the relative permeability of phase α , k is the intrinsic permeability, and T is the temperature.

The initial and side boundary conditions are defined as:

$$P_{\rm W} = P_0 + \frac{\Delta P}{\Delta z} \tag{9}$$

$$S_n = 0 \tag{10}$$

where P_w is the brine pressure at different vertical positions, calculated by initial datum pressure (P_0) and pressure gradient ($\Delta P/\Delta z$).

Usually, a CO₂ injection in the saline reservoir is controlled by several hydraulic, thermal, mechanical and thermal processes. We simulate the early time, that is, the first months of CO₂ injection. At this stage, stratigraphic trapping dominates residual, solubility and mineral trapping mechanisms (IPCC, 2005). This allows us to develop an approximate simulation procedure that neglects secondary trapping mechanisms, given the following assumptions:

- 1) The two-phase flow in porous media (geo-reservoir) obeys the generalized Darcy's law.
- 2) Mass and phase transfer between the two phases are considered.
- Dissolution of CO₂ into the brine is in thermodynamic equilibrium.
- 4) Gravity and capillary effects are taken into account.
- 5) Diffusion of CO₂ in brine is described by Fick's Law.
- 6) The initial temperature gradient is set to zero given the small thickness of the aquifer.
- 7) The interactions between fluids and rock are neglected. These include chemical reactions between fluids and rock, mechanical processes, and heat transfer between fluids and rock.
- 8) The pressure introduced from injection tests will not lead to brittle or ductile deformation of the rock.

For calculating the values of relative permeability and capillary pressure, the Brooks–Corey–Burdine model (Brooks and Corey, 1964; Burdine, 1953) is applied. Juanes et al. (2006) and Doughty et al. (2008) discussed in detail the residual trapping mechanism in $\rm CO_2$ storage reservoirs. During the $\rm CO_2$ injection phase (drainage) change in residual saturation is small and therefore the hysteretic behaviors in relative permeability–saturation and capillary pressure–saturation relationships are further neglected in our study. Additionally, variations in wettability of rock surfaces and in mineral composition are also considered negligible. In order to reduce model complexity, the residual saturation of two phases is assumed to be zero for the forward simulation:

$$k_{rw} = S_w \frac{2+3\lambda}{\lambda} \tag{11}$$

$$k_{rn} = (1 - S_w)^2 \left(1 - S_w^{\frac{2+\lambda}{\lambda}}\right) \tag{12}$$

where k_{rw} is the relative permeability of the wetting phase, and k_{rn} is the relative permeability of the non-wetting phase; S_w is the saturation of wetting phase, and λ denotes the pore distribution parameter. The capillary pressure (P_c) is calculated from:

$$P_c = P_d S_W \,^{\frac{1}{\lambda}} \tag{13}$$

where P_d is the entry pressure. The thermal conductivity is determined after Somerton et al. (1974):

$$\kappa = \kappa_{dry} + \sqrt{S_w} \left(\kappa_{wet} - \kappa_{dry} \right) \tag{14}$$

where κ_{dry} and κ_{wet} represent the dry and fully-saturated rock thermal conductivities.

2.5. Influence of CO₂ on fluid properties

For the stage prior to CO_2 injection, the pressure equation describing the single-phase system (fully brine saturated) can be written as:

$$(\phi c_w) \frac{\partial P_w}{\partial t} - \nabla \cdot \left[\left(\frac{k}{\mu_w} \right) (\nabla P_w - \rho_w g) \right] - q_w = 0$$
 (15)

where q_w is the volumetric brine injection rate, and c_w is the compressibility of brine:

$$c_W = \frac{1}{\rho_W} \frac{d\rho_W}{dP_W} \tag{16}$$

 ρ_w represents brine density, and μ_w is the dynamic viscosity of brine. Hydraulic conductivity (K_w) and specific storage (S_{sw}) are formulated as:

$$K_{W} = \rho_{W} g\left(\frac{k}{\mu_{W}}\right) \tag{17}$$

$$S_{SW} = \rho_W g(\phi c_W) \tag{18}$$

and the head change (Δh) is derived from the pressure change (ΔP_w) by:

$$\Delta h = \frac{\Delta P_w}{\rho_w g} \tag{19}$$

Unlike for shallow aquifers, in deep aquifers, density, viscosity and compressibility are affected by pressure and temperature changes, and are therefore not constant.

The injected CO_2 will change the flow properties of the twophase mixture due to its high compressibility. The flow properties of the mixture are therefore dependent on the saturation of each phase. The flow properties of the mixed-phase can be derived from a mixed-phase global pressure equation (Chen and Ewing, 1997):

$$(\phi S_w c_w + \phi S_n c_n) \frac{\partial \widetilde{P}}{\partial t} - \nabla \cdot \left[\lambda_T k \left(\nabla \widetilde{P} - \rho_d \mathbf{g} \right) \right] - q_n = 0$$
 (20)

where c_n is the compressibility of CO_2 written as:

$$c_n = \frac{1}{\rho_n} \frac{d\rho_n}{dP_n} \tag{21}$$

 λ_T is total mobility, determined by summation of individual phases' mobility (λ_w, λ_n) :

$$\lambda_T = \lambda_w + \lambda_n = \frac{k_{rw}}{\mu_w} + \frac{k_{rn}}{\mu_n} \tag{22}$$

and ρ_d is the dynamic density of mixed-phase, which is defined as:

$$\rho_d = \frac{\lambda_w}{\lambda_T} \rho_w + \frac{\lambda_n}{\lambda_T} \rho_n \tag{23}$$

In addition to the dynamic density, a static density of a mixedphase (Wang and Beckermann, 1993) is defined to describe the static parameters:

$$\rho_{\rm S} = S_{\rm W} \rho_{\rm W} + S_{\rm D} \rho_{\rm D} \tag{24}$$

In analogy to the single-phase flow equation, we can readily obtain the mixed-phase conductivity (K) and specific storage (S_s) through:

$$K = \rho_d g(\lambda_T k) \tag{25}$$

$$S_S = \rho_S g(\phi S_W c_W + \phi S_n c_n)$$
 (26)

The diffusivity of the mixed-phase (D) is given by

$$D = \frac{\lambda_T k}{\phi S_w c_w + \phi S_n c_n} \left(\frac{\rho_d}{\rho_s} \right) \tag{27}$$

According to Span and Wagner (1996), the compressibility of CO_2 is one to two orders of magnitude larger than that of the brine, which leads to a significant increase of the storage term $(\phi S_w c_w + \phi S_n c_n)$. Moreover, the compressibility of CO_2 is nonuniform within the plume and depends on pressure and temperature. The mobility of CO_2 is almost one magnitude larger than that of the brine, which may cause the conductive term $(\lambda_T k)$ to vary non-monotonically due to the nonlinear changes of the relative permeability as a function of CO_2 saturation. Thus the relationship between mixed-phase diffusivity to CO_2 saturation depends on the total mobility of the mixed-phase, on the compressibility of the two fluids, as well as on the ratio of dynamic mixed-phase density to static mixed-phase density. These aspects have to be accounted for in the following, when the mixed phase conditions are approximated by a fast standard groundwater flow model (emulator). Our

Table 1List of parameter values of numerical model based on a virtual site.

Parameter	Value	Reference	
Intrinsic permeability (k)	$1 \times 10^{-13} m^2$	Rasmusson et al. (2014)	
Porosity (ϕ)	0.2	Estimated	
Initial temperature (T_0)	340.15 K	Rasmusson et al. (2014)	
Salinity	67 g/l	Estimated	
Gravity acceleration (g)	$9.81 \text{m}^2/\text{s}$		
Residual saturation of wetting phase (S_{wr})	0		
Residual saturation of non-wetting phase (S_{nr})	0		
Initial datum pressure (P_0)	14.76 MPa	Erlström et al. (2011)	
Diffusion coefficient of CO_2 in brine (D_n)	$3 \times 10^{-9} \text{m}^2/\text{s}$	Wilke and Chang (1955)	
Rock specific heat capacity (c_r)	930 J/kg K	Robertson (1988)	
Dry thermal conductivity (κ_{dry})	3 W/m K	Robertson (1988)	
Wet thermal conductivity (κ_{wet})	4.5 W/m K	Robertson (1988)	
Entry pressure (P_d)	4000 Pa	Estimated	
Pore-size distribution (λ)	0.76	Dana and Skoczylas (2002)	
Initial averaged brine density (ρ_w)	1052.5 kg/m ³	Duan et al. (2008)	
Initial averaged brine viscosity (μ_w)	$4.2\times10^{-4}Pas$	IFC (1967)	
Initial averaged compressibility of brine (c_w)	$3.8 \times 10^{-10} \text{ 1/Pa}$	Calculated	
Initial hydraulic conductivity (K_w)	$2.46 \times 10^{-6} \text{ m/s}$	Calculated	
Initial specific storage (S_s)	$9.1 \times 10^{-7} \ 1/m$	Calculated	

hypothesis is that, through the conversion of a two-phase flow system involving two separate phases to an approximate mixed-phase flow system, transient pressure response curves can be delineated. In order to confirm this, we will compare pressure responses obtained from a full two-phase flow model and the mixed-phase emulator.

2.6. Case study

2.6.1. Virtual site

To explore the suitability of pressure tomography for the characterization of a CO2 plume, a test case is developed which is loosely oriented at the Heletz site in Israel (Table 1). The site conditions adopted in our model are mainly taken from Rasmusson et al. (2014). The proposed CO₂ storage formation is made of sandstone layers with a thickness of 15 m. It is located at a depth of 1600 m and sealed by a shale layer as the caprock. The formation pressure is 14.76 MPa with a formation temperature of 340.15 K at the aquifer bottom. CO₂ is in a supercritical state at these pressure and temperature conditions. The sandstone represents a deep saline aguifer and the salinity is assumed of 67 g/l. The rock density, intrinsic permeability and effective porosity of the sandstone are set to $25\overline{50}$ kg/m³, 1×10^{-13} m² and 0.2, respectively. These values are representative for deep CO2 storage formations composed of sandstone (e.g., Hovorka et al., 2004). Entry pressure of sandstone can cover a broad range (e.g., Krevor et al., 2011); here we choose a moderate value of 4000 Pa. The thermal properties of the rock, including heat capacity and thermal conductivity, are estimated according to Robertson (1988).

2.6.2. Numerical model

The sandstone formation is simulated in a two-dimensional numerical model as a homogeneous, isotropic aquifer with a thickness (*d*) of 15 m (Fig. 1). The lateral dimension (*x*-direction) of the model is 580 m. A simplified two-dimensional model is appropriate to demonstrate the effectiveness of the inversion techniques as has been demonstrated by Yeh and Zhu (2007) or Xiang et al. (2009), but it neglects the three-dimensional nature of the flow pattern in a real injection system. For characterizing three-dimensional non-uniform plume spreading in the field, at least three wells would be required.

The initial brine pressure distribution in the model is hydrostatic and brine is the only liquid phase. The supercritical CO_2 is injected at the center of the model. The observation well is placed at a distance of 50 m, which is a common distance for well pairs at CO_2

pilot sites (e.g., Wiese et al., 2010). The thickness of each layer is set to be 0.6 m and held constant throughout the simulation. Between the two wells, a horizontal discretization of 0.5 m is chosen, with a progressive refinement to 0.09 m toward the injection well. Outside of the target area, the grid size is increased exponentially with the largest grid size of 40 m at the distant boundaries. This yields a discretization of 287 and 25 grid cells in horizontal and vertical directions respectively, with 7175 grid cells in total.

The open source code PFLOTRAN (e.g., Hammond et al., 2014) is employed for the two-phase non-isothermal supercritical CO₂-brine flow simulation. The density of the brine/CO₂ mixture is calculated based on the state equation from Duan et al. (2008), and the viscosity of brine computation follows the IFC (1967). The solubility equation for describing CO₂ in brine is taken from Duan and Sun (2003). We apply the state equation developed by Span and Wagner (1996) to obtain the density and the method proposed by Fenghour et al. (1998) for the viscosity of supercritical CO₂.

2.6.3. Cross-well testing at different stages

In the numerical model, several cross-well experiments are conducted in a tomographic configuration to derive space filling pressure response curves. These experiments are all configured equally, that is 5×5 screens at the source and the receiver. The length of each injection interval is 0.6 m. Injection of CO_2 occurs at different times at each of these intervals (Fig. 2 and Table 2). The injection of CO_2 over discrete time intervals facilitates time-lapse analysis and is intended to reveal how broad the application window of pressure tomography is. We also distinguish three different durations (short, medium, long) of these stages, since the period of injection is an important factor in the injection model and its role for the inverted results unknown. The four studied stages are characterized as follows:

Stage 1: Cross-well multilevel brine injection tests. Prior to CO_2 injection, five multilevel brine injection tests at different depths are simulated and the pressure response curves recorded at the

Table 2 Duration of the four stages $(\Delta t_1 - \Delta t_4)$ given short, medium and long CO_2 storage periods.

Injection time	Stage 1	Stage 2	Stage 3	Stage 4	Total duration (h)	
	Δt_1 (h)	Δt_2 (h)	Δt_3 (h)	Δt_4 (h)		
Short	70	120	240	36	466	
Medium	70	240	240	45	595	
Long	70	360	240	54	724	

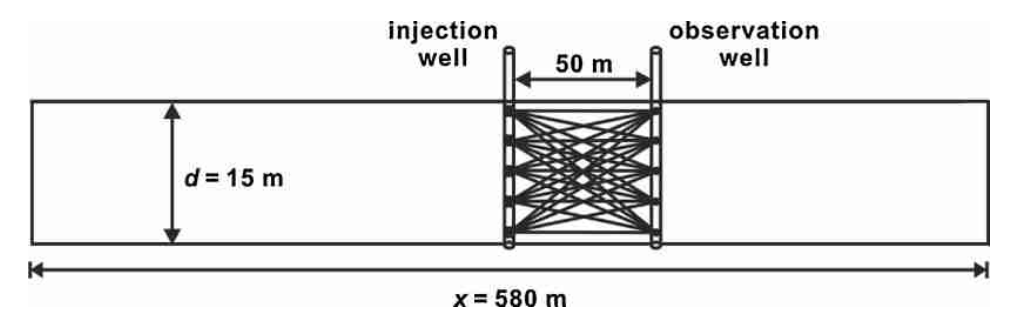


Fig. 1. Configuration of the source (injection well) and the receiver (observation well) in a cross-sectional numerical model.

observation well. The formation is fully brine-saturated without any CO_2 . The brine is injected from bottom to top sequentially at a rate of $Q_w = 0.001$ kg/s. Between two subsequent injections (interval of 2 h each), a recovery period of 15 h is simulated until the pressure has recovered to initial conditions. Thus, the total duration of this stage is $70 \text{ h} (\Delta t_1)$. Pressure tomography at this pre-injection stage provides a reference, which can be compared with the pressure signals obtained during CO_2 injection at a later stage.

Stage 2: CO_2 injection. At this stage, CO_2 sequestration is initiated and conducted for a short period of Δt_2 = 120 h, a medium period of 240 h or long period of 360 h. CO_2 is injected at a rate of Q_c = 0.02 kg/s over the entire depth at the source well, which creates a two-phase system in the deep aquifer. No cross-well experiments are carried out at this stage.

Stage 3: Shut-in after CO_2 injection. This stage represents a recovery period after the previous injection stage. The pressure recovers for Δt_2 = 240 h to its initial hydrostatic state. Thus, hydrostatic pressure conditions are reinstated for the calibration procedure at a later stage.

Stage 4: Cross-well multilevel CO_2 injection tests. Analogous to the initial multilevel brine injection tests (stage 1), and with the same set-up, CO_2 is now used as a medium for cross-well testing ($Q_c = 0.02 \text{ kg/s}$). In contrast to the brine injection, shorter recovery periods are applied and thus the formation pressure does not fully recover at this stage. This is to avoid long relaxation phases and the associated transient effects induced by CO_2 migration (e.g., changes in plume shape) during the tomographic analysis. In our example,

we set equal injection and recovery periods and adjusted them to the injected volume of CO_2 (stage 2), with 4 h (short), 5 h (medium) and 6 h (long) (Table 2). Pressure responses derived during this stage are used to reveal the modified in-situ flow properties and by this localize the CO_2 plume.

3. Results and discussion

3.1. Forward modeling results

Fig. 3 shows the simulated CO_2 plume development for the four stages assuming short, medium and long injection in stage 2. The snapshots of CO_2 saturation distribution were taken at the end of the respective stage. The maximum CO_2 saturation within the plume reaches around S_n = 0.6. As expected, the cross-well-testing by injecting brine does not show any effect in stage 1. As soon as CO_2 is injected, a plume evolves and migrates laterally and upwards toward the top of the aquifer due to buoyancy effects. Because of the high pressure at the source well during injection the lateral plume extension is most pronounced there. During recovery in stage 3, gravity forces become the main driver for CO_2 and the plume develops toward the top of the aquifer. At stage 4, little change in the plume shape and in saturation is observed. This is an important observation, since it demonstrates that during the final cross-well CO_2 injection tests the plume shape can be assumed to be constant.

In the following, we focus on the multilevel-injection experiments for tomographic analysis. The pressure responses recorded

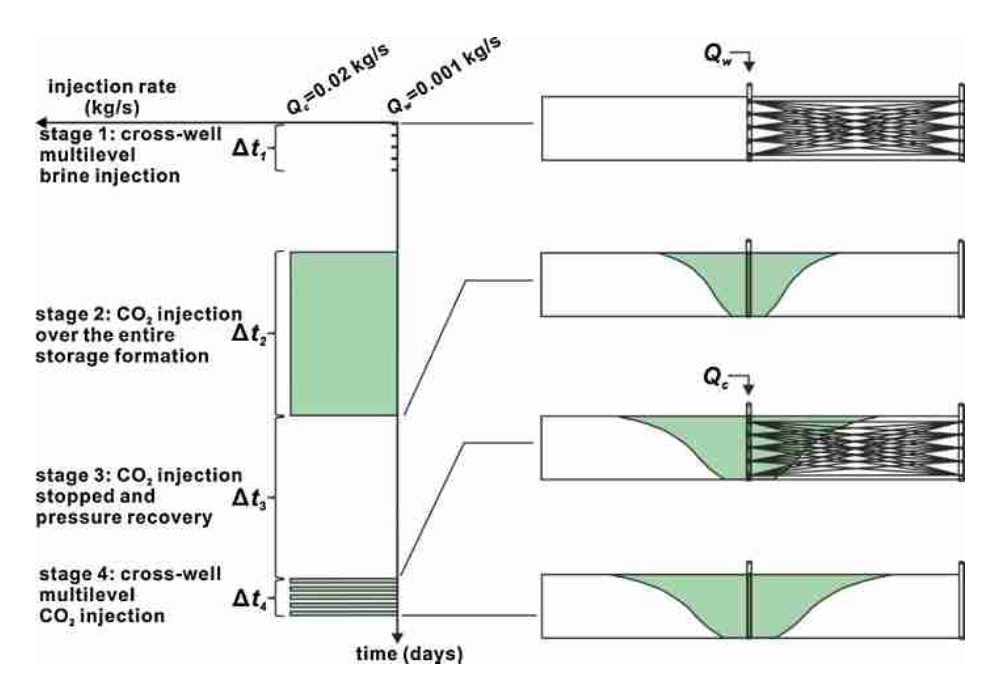


Fig. 2. Time sequence of the four sequentially modeled operational stages with cross-well testing before and after CO_2 injection.

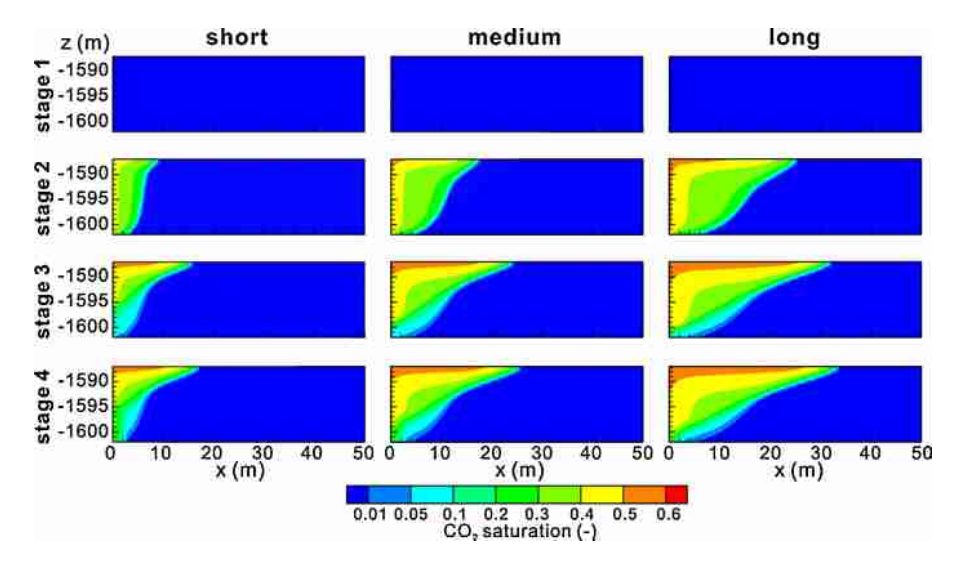


Fig. 3. CO₂ plume evolution according to its saturation during short, medium and long-term CO₂ injection, illustrated for stages 1-4 (see Fig. 2).

at the observation well at the initial and last stage are presented in Fig. 4. Since these responses are similar for the five receiver levels, we only show the results for the central screen. The sequential multilevel brine injection yields uniform responses, which are all similar for the homogeneous aquifer (Fig. 4a). The recovery period of 15 h is sufficient to recover to the initial system pressure distribution such that no response is influenced by the previous one.

Fig. 4b depicts the recorded pressure during all following stages, ending with the final multilevel CO_2 injection. It shows that after the start of CO_2 injection, a maximum pressure of P_w = 15.8 MPa is reached within the aquifer. The same pressure is obtained for different CO_2 storage times (short, medium, long). During recovery (stage 3), the pressure returns to the initial hydrostatic level. During subsequent multilevel injection, the pressure recovery is incomplete and each new injection contributes to the recorded pressure. Due to the increased extension of CO_2 plume and high compressibility of CO_2 , pressure responses are less well pronounced after longer injection and they decline during sequential multilevel testing.

3.2. Comparison of pressure responses from proxies and full models

Our strategy is to approximate the complex full two-phase model with a simplified single-phase proxy and by this facilitate fast iterative model calibration. The suitability of the proxy (implemented in MODFLOW) is assessed by comparing results with those of the two-phase simulations with PFLOTRAN. In the following, the simulated pressure changes at the observation well are transferred to head changes via Eq. (19).

First, the head changes from the brine injection tests at stage 1 prior to CO_2 storage will be compared. In the proxy, the hydraulic parameters are fixed to the initial values of the full model as specified in Table 1. Potential density and viscosity changes due to pressure and temperature variations are neglected. Comparison between both models in Fig. 5 shows only small differences, and thus the proxy is considered a viable tool for the inversion.

The effect of viscosity, density and compressibility on hydraulic conductivity as defined in Eqs. (17) and (21) can explain the small discrepancies between both curves. The two-phase simula-

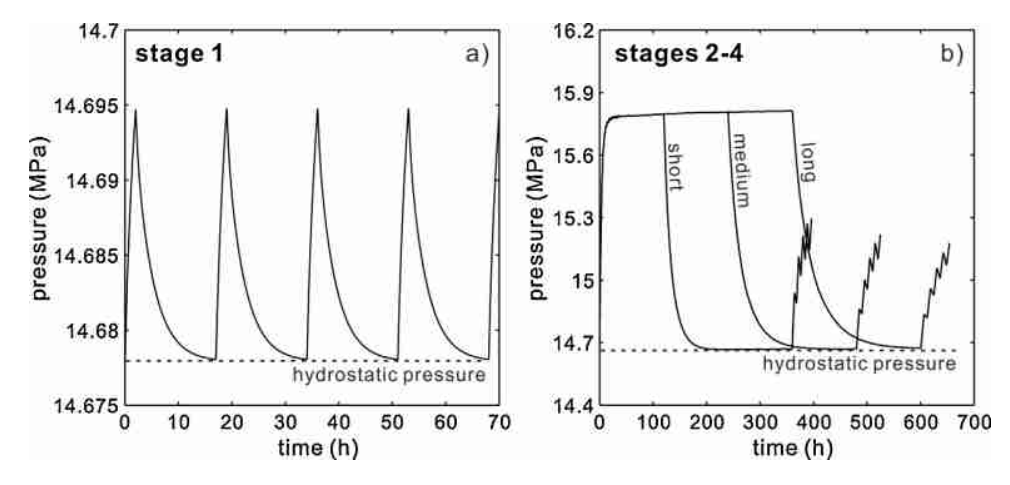


Fig. 4. Pressure changes for different stages: (a) pressure response curves from stage 1; (b) pressure response curves from stages 2–4 covering storage, recovery and multilevel-testing.

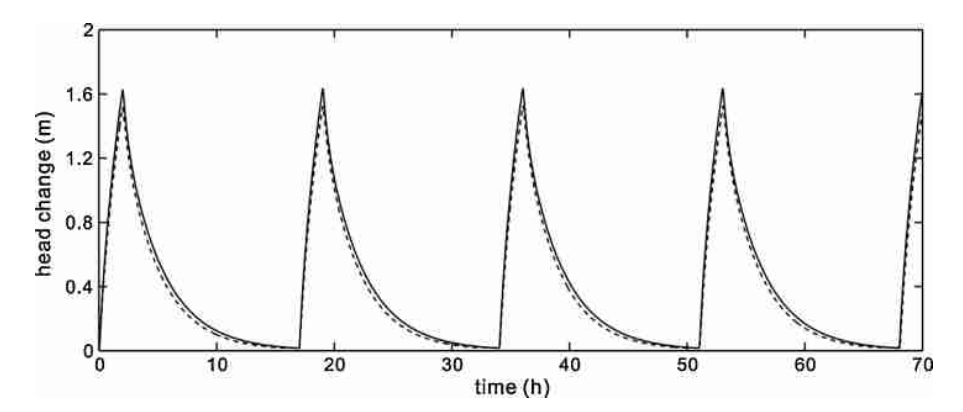


Fig. 5. Comparison of head changes from full model (solid line) and proxy (dotted line).

tion showed minor changes on the order of 1.8×10^{-9} Pa s in the viscosity of water. Therefore, a mean value of 4.2×10^{-4} Pa s was chosen. In contrast, density and compressibility of the brine vary more strongly due to induced pressure and temperature changes. These also in turn affect hydraulic conductivity and specific storage. According to Eq. (18), specific storage is not determined by brine density, but relates to the term $\frac{d\rho_{W}}{dP_{W}}$. Referring to the state equation of Duan et al. (2008), this term equals to 4×10^{-7} kg/(m³ Pa) for our simulation conditions. Thus, specific storage can be treated as a constant. In contrast, hydraulic conductivity is determined by brine density. The pressure increase leads to a higher brine density in the full two-phase model. Consequently, hydraulic conductivity increases as well, which could cause the larger head changes in the full model compared to the proxy.

Analogous to the single-phase proxy of stage 1, a mixed phase proxy (emulator) for simulating the head changes from multilevel CO₂ injection (stage 4) is introduced. It is based on the following assumptions: The process is assumed isothermal. A single integrated value of CO_2 compressibility c_n exists, which can minimize the discrepancies between the results from full two-phase model and mixed-phase proxy. The two phases in the aquifer, brine and CO₂, are slightly compressible. Therefore, density values of brine and CO_2 (ρ_w and ρ_n) are set constant according to the values at the beginning of the injection. In the emulator, compressibility of brine and CO_2 (c_w and c_n) does not change, calculated from the state equation of two fluids. Capillary pressure (P_c) is neglected, so that the liquid pressure (P_w) equals to the gas pressure (P_n) and the global pressure (\widetilde{P}) . Furthermore, saturation changes are ignored, so that pressure changes are calculated solely from the global pressure equation (Eq. (20)). Finally, viscosity of the two phases (μ_w and μ_n) is set constant.

The mixed-phase flow properties derived from Eqs. (25) and (26) are utilized as the input parameters for the emulator. At stage 4, the state equation of CO₂ reveals that the density of CO₂ as a function of the pressure ($\frac{d\rho_n}{dP_n}$) changes from 4×10^{-5} to 5.3×10^{-5} kg/(m³ Pa) for a pressure range from 14.01 to 15.51 MPa at 340.15 K, respectively. Through the transformation from Eqs. (25) to (27), the gas saturation values at the start of the tests were transferred to mixed-phase conductivity, specific storage and diffusivity.

The transferred mixed-phase flow parameters vs. CO_2 saturation are plotted in Fig 6. Fig. 6a shows that the maximum mobility of CO_2 , λ_n , is one order of magnitude higher than that of water, which is due to the difference in viscosity of these two phases. The mixed-phase hydraulic conductivity K spanning a range from 9.8×10^{-7} to 1.3×10^{-5} m/s (Fig. 6d) is controlled by the total mobility λ_T and dynamic mixed-phase density ρ_d (Fig. 6b and c). The result-

ing conductivity does not change monotonously, and shows minor variability within the saturation (S_n) range of 0–0.5. When CO_2 saturation rises from 0 to 0.22, the conductivity declines due to a decrease in brine mobility and a dynamic mixed-phase density. When CO_2 saturation is larger than 0.22, the conductivity increases along with the growing CO_2 saturation.

Specific storage (S_s) rises with CO_2 saturation, since the introduced compressibility is much larger than the initial value for the brine. The range of specific storage varies from 9.1×10^{-7} to 9.1×10^{-5} 1/m (Fig. 6e, blue line) when $\frac{d\rho_n}{dP_n} = 4 \times 10^{-5}$ kg/(m³ Pa) and it changes from 9.1×10^{-7} to 1.2×10^{-4} 1/m (Fig. 6e, red line) when $\frac{d\rho_n}{dP_n} = 5.3 \times 10^{-5}$ kg/(m³ Pa). Being the ratio of conductivity to specific storage, the curve delineating the mixed-phase diffusivity in Fig. 6f does not show a monotonous behavior either. Overall, the diffusivity is lower than that of the CO_2 -free aquifer, which is 2.7 m²/s.

The key point when designing the emulator is to determine a robust integrated value of $\frac{d\rho_n}{dP_n}$, which shows the same pressure responses as the full model. In the pressure tomographic approach, especially the early parts of these responses (early time diagnostics) are examined. Therefore, we tested in a plausible range of $\frac{d\rho_n}{dP_n}$ from 4×10^{-5} kg/(m³ Pa) to 5.3×10^{-5} kg/(m³ Pa) and compared the stage 4 pressure response curves for variable injection times and injected CO₂ volumes (Fig. 7). For the short, moderate and long scenarios, values of 4.9×10^{-5} kg/(m³ Pa), 5.1×10^{-5} kg/(m³ Pa) and 5.2×10^{-5} kg/(m³ Pa) respectively, were considered to be most suitable (Fig. 7, black dotted line).

In the following, the results from modeling the evolution of mixed-phase conductivity, specific storage and diffusivity within the plume is shown for the four stages considered. This is of particular interest, because the emulator is only capable of simulating a pseudo-mixed single phase. In Figs. 8–10, the forward modeling data of the full model are visualized, which are derived from the CO₂ saturations at different times (see Fig. 3). In this simulation, the variability of mixed-phase conductivity (Fig. 8) is within 1×10^{-6} and 4.5×10^{-6} m/s and hence, is quite small. The largest values occur at the top of the plume where the saturation of CO₂ is at a maximum (Fig. 3). Consistent with the transformation function (Fig. 6d), the smallest values appear where the CO₂ saturation is below 0.22.

Similar to the hydraulic conductivity, the mixed-phase specific storage is correlated with the CO_2 saturation (Fig. 9) but computed values span over two orders of magnitude from 1×10^{-6} to 1×10^{-4} 1/m. The diffusivity (Fig. 10) can be determined from the subsequent travel-time based inversion. As inferred from Fig. 6f, in the plume, the mixed-phase diffusivity declines in contrast to

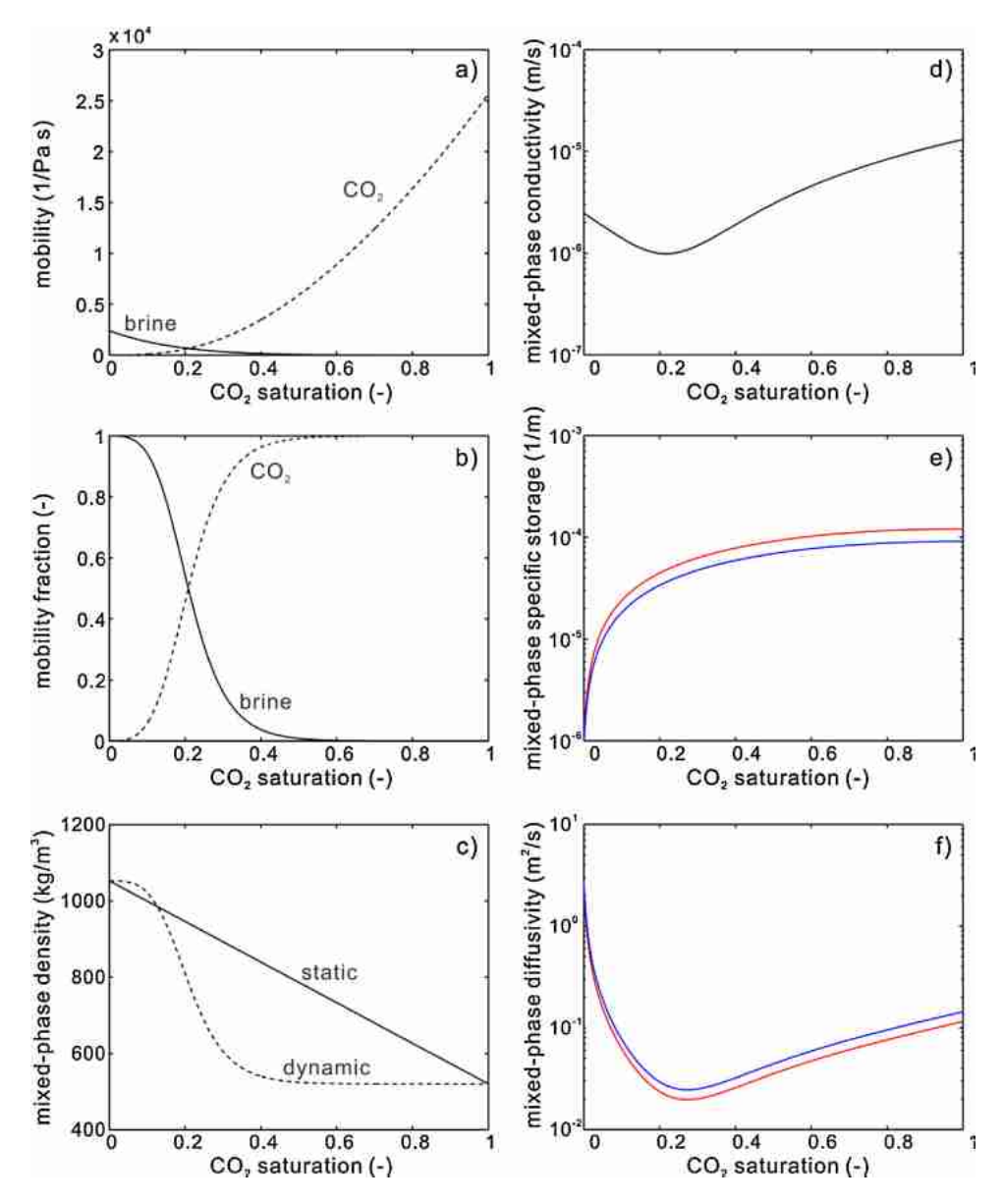


Fig. 6. Flow properties vs. CO₂ saturation: (a) mobility of two phases; (b) mobility fraction of two phases; (c) mixed-phase density; (d) mixed-phase conductivity; (e) mixed-phase specific storage; (f) mixed-phase diffusivity (blue lines: $\frac{d\rho_n}{dP_n} = 4 \times 10^{-5} \text{ kg/(m}^3 \text{ Pa)}$; red lines: $\frac{d\rho_n}{dP_n} = 5.3 \times 10^{-5} \text{ kg/(m}^3 \text{ Pa)}$). (For interpretation of the references to color in the text, the reader is referred to the web version of this article.)

the ambient aquifer ($D = 2.7 \text{ m}^2/\text{s}$). However, toward the top where CO_2 saturation exceeds 0.22, the diffusivity slightly increases again, following its relationship with the conductivity.

3.3. Eikonal based inversion

3.3.1. Early time diagnostics

With the full numerical model of the virtual site, we cannot only predict the evolution of the CO_2 plume, but also the pressure responses from the tomographic tests with brine (stage 1) and CO_2 injection (stage 4). In the following we will focus on the travel time diagnostics used for the eikonal inversion. Afterwards, the emulator is used for the calibration of the response curves. In the discussion of the results, we name the five source intervals at the central injection well S1–S5 from bottom to top, and the five receiver intervals at the observation well R1–R5.

In a first step, the head changes and their first time-derivatives are derived from the multilevel brine injection tests during stage 1 (Fig. 11a and e). The results are identical in each source-receiver

combined pattern and thus only the result of one single injection test is presented. As shown in Fig. 11a, the head increases by 1.62 m during the 2 h of injection but does not reach steady state. The peak travel time appears after 411 s, with some oscillation in the derivative. The values of the more robust early time diagnostics, t-10%, t-20%, t-30%, t-40% and t-50%, are 21 s, 45 s, 72 s, 90 s and 113 s, respectively.

In a second step, travel times from stage 4 were computed by the first time-derivative of the head changes. The trends in the head changes and associated first time-derivatives are similar at all observation points (R1–R5). Fig. 11b–d illustrates the head changes from the multilevel CO₂ injection tests at the bottom of the observation screen (R1), and Fig. 11f–h shows the corresponding first time-derivatives of the head changes. From S1 to S5, the decreasing head changes reflect the growing influence of CO₂ accumulating at the top of the aquifer. For the inversion, considering the initially steep slope of the derivative curves, the early travel time diagnostics seem favorable. These diagnostics are smallest at the bottom observation screen (R1) and increase toward R5 (not shown). A

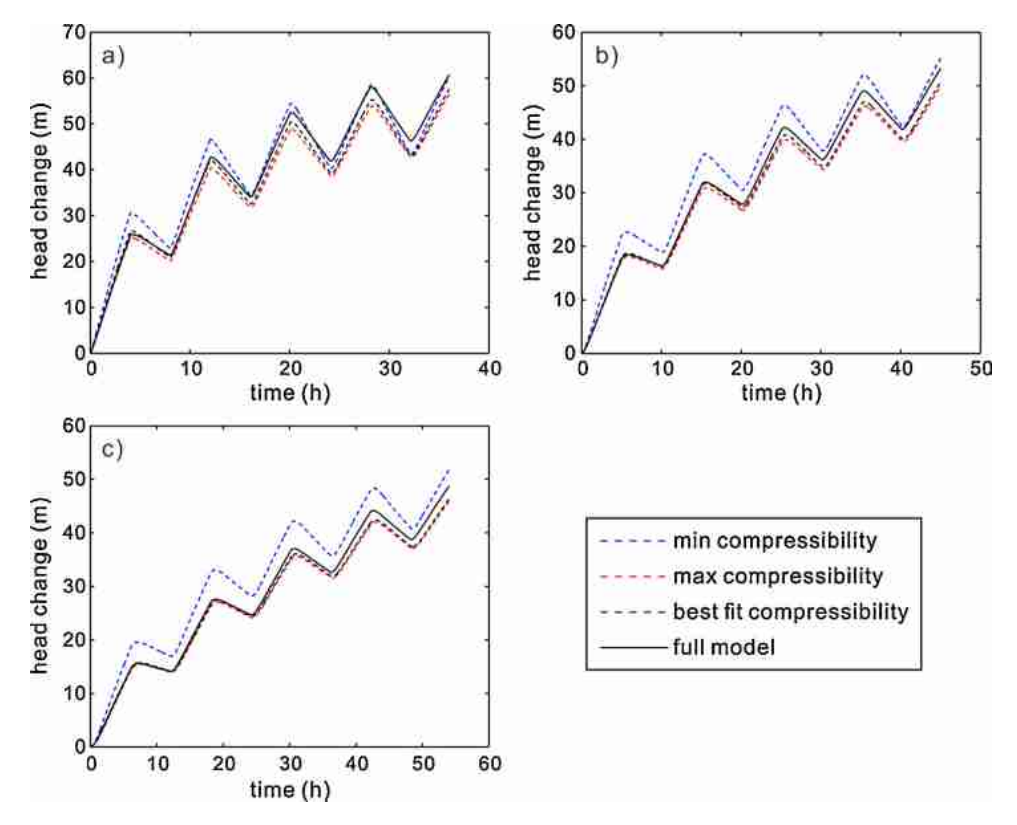


Fig. 7. Head comparison of full model and emulator for different periods of CO₂ injection during stage 4: (a) short, (b) medium, (c) long time injection.

comparison of the head change and first derivative curves after the three different CO_2 injection periods reveals that the developed plume also lowers the head changes and their first derivative values for a given source-receiver configuration. Accordingly, the early travel time diagnostics show a delay when the CO_2 injection period increases.

With the insight from Fig. 11, we focus on the early time diagnostics, which are more informative than peak times. We selected a moderate value of t-20% for the inversion process. In fact, the other early time diagnostics can offer similar structural information of the inverted tomograms since they equally show a consistent change for each source-receiver pattern. The main difference from

using different diagnostics would be seen in the absolute values of inverted diffusivity and thus it is not further discussed here.

3.3.2. Diffusivity tomograms

With the recorded travel time diagnostics (*t*-20%), eikonal based inversion can be employed to obtain a diffusivity tomogram. We applied the Geotom code (Jackson and Tweeton, 1996) for the inversion by implementing the SIRT (simultaneous iterative reconstruction technique) solver (Gilbert, 1972). A staggered grid technique (Vesnaver and Böhm, 2000) was applied to increase the nominal resolution of the tomograms. Without this technique only

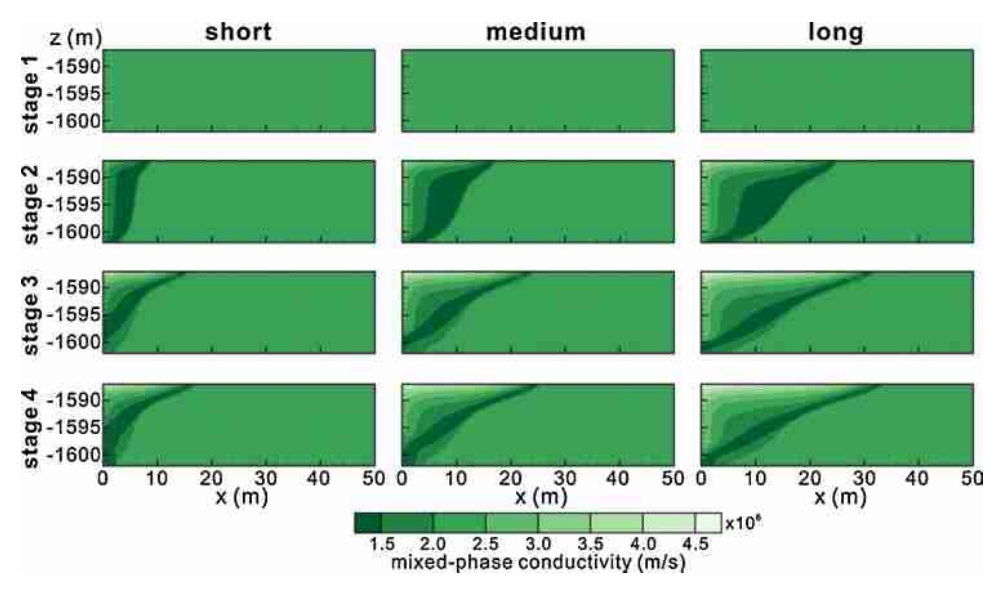


Fig. 8. Mixed-phase hydraulic conductivity evolution during short, medium and long-term CO₂ injection, illustrated for stages 1–4 (see Fig. 2).

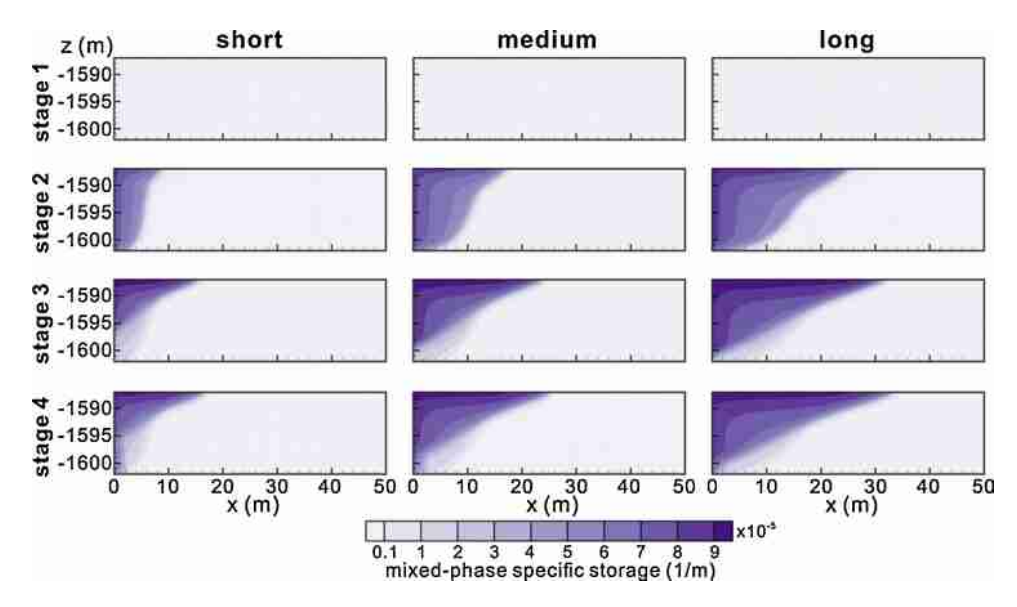


Fig. 9. Mixed-phase specific storage evolution during short, medium and long-term CO₂ injection, illustrated for stages 1-4 (see Fig. 2).

Table 3Calibration result and transferred CO₂ saturation.

	Calibrated S _s (1/m)	Calibrated K (m/s)	S_n (in range) (–)	S_n (calculated) (-)	S_n (true) ($-$)
Pre-injection	8.6×10^{-6}	2.24×10^{-6}	0	0	0
Short injection	4.02×10^{-5}	-	0.18-0.25	0.21	0.22
Medium injection	6.27×10^{-5}	-	0.3-0.43	0.35	0.33
Long injection	5.83×10^{-5}	_	0.27-0.39	0.32	0.32

a coarse tomogram with a grid of 5 columns and 4 rows would be feasible based on the number of source and receiver intervals. The number of unknowns is adapted to the number of available source-receiver configurations, and thus the inversion problem can be approximately considered as an "Even-Determined Problem" (Brauchler et al., 2003, 2007). In the staggered grid approach, instead of one grid, multiple shifted grids were applied for separate inversion, which together can be arithmetically averaged into a high-resolution tomogram. The shifting step sizes in *x*-direction and in *z*-direction were 2 m and 1.875 m respectively, and a final diffusivity tomogram with 25 columns and 8 rows was obtained

from 10 individual inversions. The inversion was stopped once the error between calculated and measured travel times was convergent. This procedure was applied to the multilevel brine-injection experiment in stage 1, and to the multilevel CO_2 injection (stage 4).

As a reference, the diffusivity tomogram of stage 1 was constructed. Fig. 12a shows that the inverted diffusivity (D) varies only within a small range from 2.84 to 2.94 m²/s. This means the homogeneity of the aquifer is nicely reflected by the tomogram. As it is common for such eikonal inversion, absolute values are not well reproduced (Jiménez et al., 2013). Here the mean value of 2.9 m²/s is higher than the "true" value for the aquifer ($2.7 \, \text{m}^2/\text{s}$). Also, the

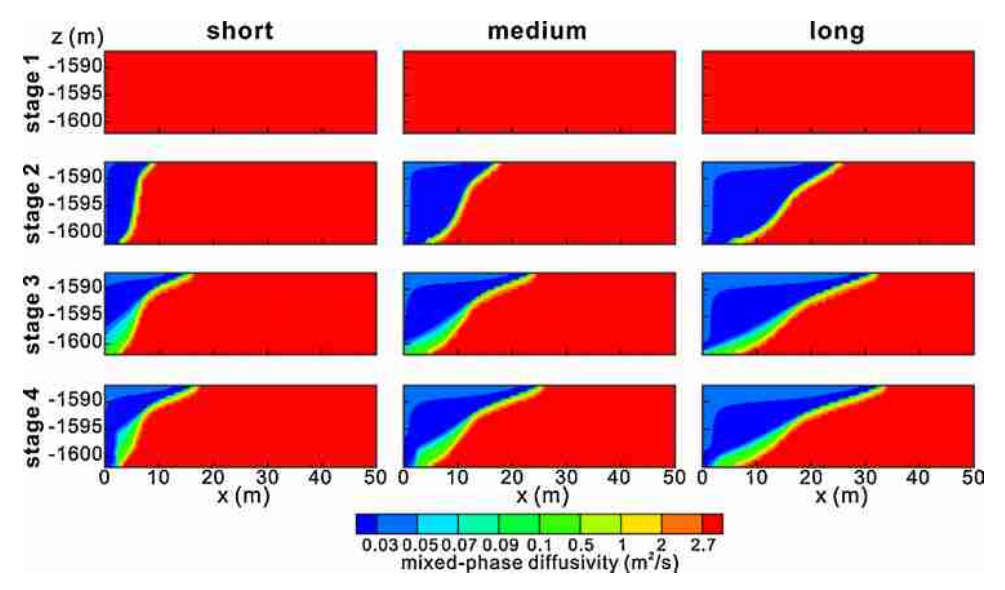


Fig. 10. Mixed-phase diffusivity evolution during short, medium and long-term CO₂ injection, illustrated for stages 1–4 (see Fig. 2).

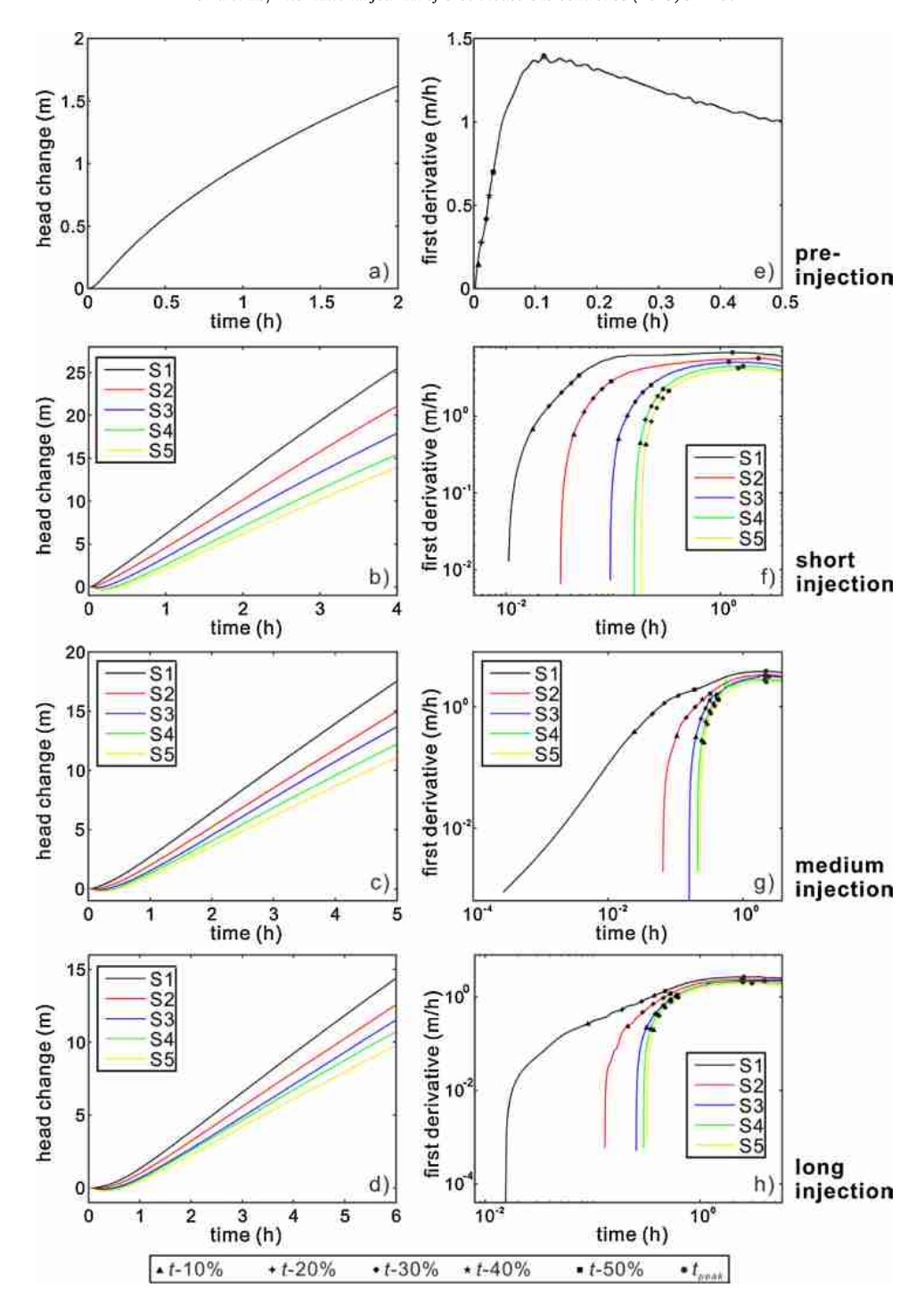


Fig. 11. Head changes and first derivatives of five injection period in R1 before CO₂ injection, and during short, medium and long-term CO₂ injection.

null space energy was calculated, and the obtained reliability map shows that the values at the upper boundary are the least reliable. The unreliable values and the slight variability of *D* are caused by the non-uniform trajectory density. In such cross-well tests, trajectory density is larger in the model center than at the top and bottom (Hu et al., 2011) and this is reflected by the minor variability of *D* in the central area of the tomogram.

The diffusivity tomograms of stage 4 after short, medium and long injection periods are depicted in Fig. 12b–d. A common feature in all tomograms is the low diffusivity area at the injection well, which is consistent with the CO₂ plume zone simulated by the full two-phase model (PFLOTRAN simulation). It can be seen that the tomograms after different injection periods show the evolution of

the CO₂ plume. Again, absolute D values deviate substantially from the simulated "truth". The inverted range of D values is about half of the true range. Particularly in the CO₂-free ambient aquifer, which appears in red color in the true model, D is strongly underestimated. In this part of the aquifer, the arithmetic mean values of D are 0.97, 0.55, and 0.14 m²/s for short, medium and long injection periods, respectively, which are all below the "true" value (D=2.7 m²/s). These results demonstrate that the derived tomograms are suitable to capture structural information and thus to identify the shape of the plume. However, the inverted values of D are not appropriate for computing the CO₂ saturation. This requires full pressure response calibration, which is pursued below.

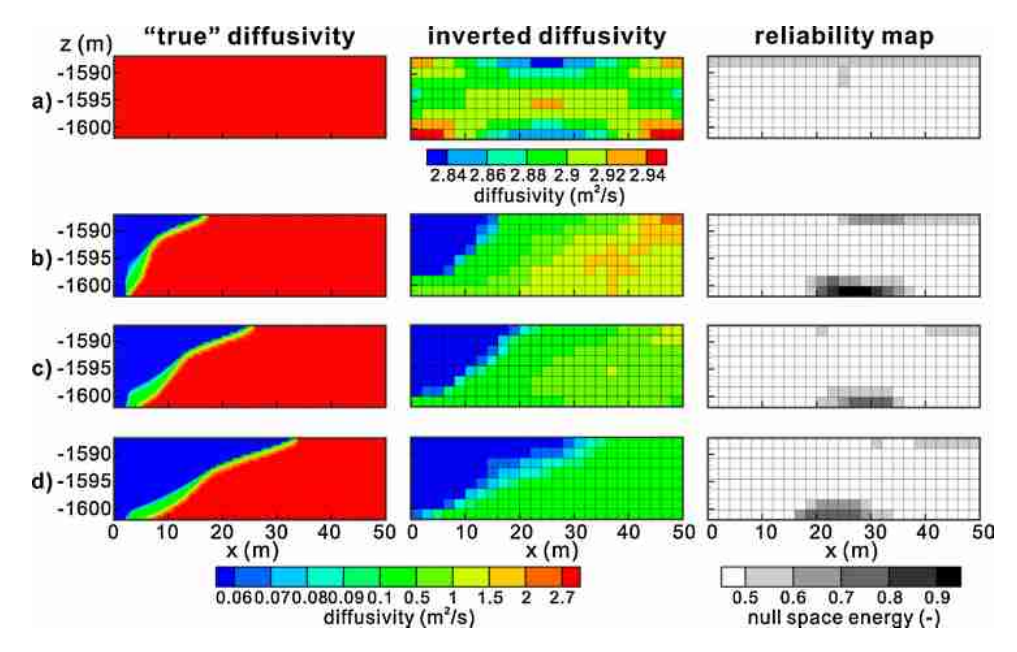


Fig. 12. True and inverted diffusivity tomograms with reliability maps after stage 4 in different times: (a) pre-injection; (b) short injection; (c) medium injection; (d) long injection.

The computed null space energy maps (Fig. 12, third column) show larger values (greater than 0.5) at the upper right corner and the bottom of the cross section for all injection periods. However, these unreliable pixels or zones are outside the plume area, and hence a localization of the plume was possible.

3.4. Clustering and full signal calibration

As a standard data partitioning method, k-means clustering is applied to cluster the tomograms obtained after CO_2 injection, and by this, to distinguish between plume and ambient aquifer pixels. k-means clustering classifies the data according to their distance to the nearest centroid. The two centroids of each cluster were determined by histogram analysis, and kept constant for all injection periods ($D = 0.055 \, \mathrm{m}^2/\mathrm{s}$, $0.13 \, \mathrm{m}^2/\mathrm{s}$). In order to account for data reliability, the cluster analysis was only based on pixels with null

space energy smaller than 0.5. The positions with greater values were filled up by nearest neighbor interpolation of the adjacent cluster, which was here always the one representing the $\rm CO_2$ -free ambient aquifer.

At this point, we set up one homogeneous aquifer model for stage 1, representing the pre-injection conditions, and for each injection period a clustered model with zonal structure is available. This facilitates a two-step full pressure signal calibration (using PEST), assuming that the zones represent homogeneous areas. From calibrating the pre-injection model, a hydraulic conductivity of 2.24×10^{-6} m/s and specific storage of 8.6×10^{-6} 1/m are determined. These values are also valid for the ambient aquifer after CO₂ injection, and thus assigned to this zone in the stage 4 models.

Recalling the relationships between flow properties and CO₂ saturation (Fig. 6), calibrating the mixed-phase specific storage of

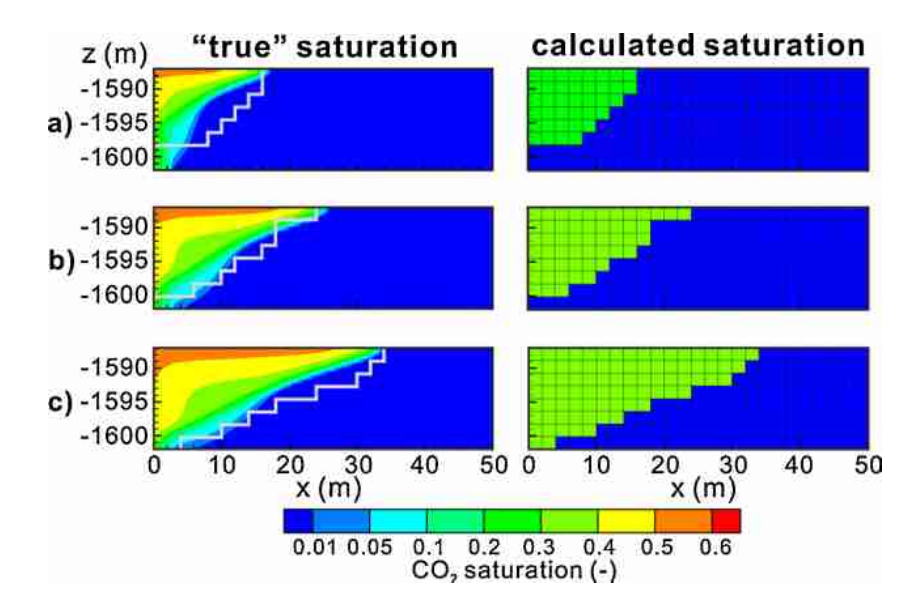


Fig. 13. Calculated saturation compared with "true" values after stage 4 in different times: (a) short injection; (b) medium injection; (c) long injection. The grey line in "true" saturation graphs delineates the inverted plume shape.

the emulator is best suited for estimating CO_2 saturation due to the monotonous relationship. Moreover, the introduced CO_2 phase disturbs the mixed-phase specific storage much more than mixed-phase conductivity. As an additional argument, Wu et al. (2005) pointed out that the early head changes are more sensitive to specific storage compared to hydraulic conductivity. Thus, only the specific storage of the plume was calibrated, assuming that the hydraulic conductivity can be set to be uniform for the entire model. In this case, relative permeability curves have no impact on the inversion.

The first three stress periods of the head changes were utilized for the calibration since they display minor differences between the results from the full model and the proxy. The calibrated specific storage values for the plumes of three injection periods are shown in Table 3. The calibrated values indicate that the specific storage of the plume is almost half a magnitude larger than that of the original aquifer. Referring to the changes of $\frac{d\rho_n}{dP_n}$, the CO₂ saturation inferred from specific storage can vary from 0.18 to 0.25, 0.3 to 0.43, and 0.27 to 0.39 for short, medium and long injection periods, respectively. If we take the mean value of $\frac{d\rho_n}{dP_n}$ to calculate the CO₂ saturation, then the final values of CO_2 saturation are 0.21, 0.35, and 0.32. These values agree very well with the arithmetic mean of the "true" saturation values within the clustered structure (0.22, 0.33 and 0.32) (Table 3). In a last step, we visualize the plume shapes and compare the calculated CO₂ saturation within the plume with the "true" saturation distribution (Fig. 13). The figure shows that the plume, especially the edge of the plume, can be localized by the inversion and clustering approaches.

4. Conclusions

Monitoring techniques are essential for improving the safety and optimizing the operation of CO_2 storage sites. A novel approach, the time-lapse pressure tomography inversion, is developed and successfully demonstrated for monitoring the CO_2 plume evolution in underground storage reservoirs. This method is based on principles of hydraulic tomography, which is most commonly used for the characterization of shallow aquifers. The latter utilizes hydraulic pressure signals from multiple sources and receivers for a spatial reconstruction of heterogeneity. Since a CO_2 plume directly influences the hydraulic properties and induces an apparent heterogeneity, a concept similar to hydraulic tomography can be adopted for reconstructing the shape of the plume. By inspecting the transient behavior of the plume through repeated pressure applications, a time-lapse pressure tomography is obtained.

We have shown the feasibility of the proposed investigation method by simulating a realistic deep CO₂ storage site in a homogeneous saline aquifer. Pressure signals are simulated by both brine and CO₂ injection and recorded between two wells at different levels. The signals are inverted by a fast but approximate travel time based tomographic procedure, which offers a first insight into the plume shape and how it evolves over time. We demonstrated that the information from the pressure signals could be used for full calibration of a process-based numerical model. This provides the opportunity for resolving not only the shape of the plume, but also for directly determining the spatial distribution of the non-wetting phase saturation. In the case study presented here, the estimated values of saturation are consistent with those computed explicitly in simulated CO₂ injection scenarios. This good agreement holds even though a simplified single-phase model or "emulator" was used for the calibration. The approximation of multi-phase processes with a simplified single-phase numerical model appears sufficient to capture the conditions relevant for the tomographic inversion. By this, a computationally efficient full signal based

inversion is possible without requiring a complex multi-phase simulation.

One fundamental advantage of the new method is that it requires only a doublet well configuration, i.e., an injection and an observation well, and, therefore, can be applied to a large range of geological reservoirs. Another advantage is that the method is fast (from a few minutes to hours) and rather inexpensive from a computational point of view, as it requires the injection of only small fluid (water, brine, CO₂) volumes. Note that no fluids are extracted and have to be disposed of. Nevertheless, for multilevel injection sequences, packers must be installed which may entail additional costs. In principle, the application window of the proposed pressure tomography is not restricted to homogeneous and isotropic aguifers only. This will be further explored in future work focusing on the transient changes in the reservoir in the time-lapse framework. A crucial point for feasibility in practice will be that the pressure signals reach good spatial resolution, and that a sufficiently high signal-to-noise ratio is achieved. This will determine the application scale, which is expected to be smaller than, for example, that of seismic tomography, but with better resolution at the small scale. Ideally, for real-time monitoring of a CO₂ plume, the time-lapse pressure tomography approach is combined with complementary tracer testing or geophysical techniques.

Acknowledgements

We would like to acknowledge the funding from the EU 7th Framework Programme FP7 under grant number 309067, project TRUST. We also thank the anonymous reviewers for their fruitful comments and Rui Hu for the discussions on inversion techniques.

References

- Ajo-Franklin, J.B., Peterson, J., Doetsch, J., Daley, T.M., 2013. High-resolution characterization of a CO₂ plume using crosswell seismic tomography: Cranfield, MS, USA. Int. J. Greenhouse Gas Control 18 (10), 497–509, http://dx.doi.org/10.1016/j.ijggc.2012.12.018
- Bachu, S., Adams, J.J., 2003. Sequestration of CO₂ in geological media in response to climate change: capacity of deep saline aquifers to sequester CO₂ in solution. Energy Convers. Manage. 44 (20), 3151–3175, http://dx.doi.org/10.1016/S0196-8904(03)101-8
- Bergmann, P., Schmidt-Hattenberger, C., Kiessling, D., Rücker, C., Labitzke, T., Henninges, J., Baumann, G., Schütt, H., 2012. Surface-downhole electrical resistivity tomography applied to monitoring of CO₂ storage at Ketzin, Germany. Geophysics 77 (6), B253–B267, http://dx.doi.org/10.1190/geo2011-0515.1
- Bohling, G.C., Zhan, X., Butler, J.J., Zheng, L., 2002. Steady shape analysis of tomographic pumping tests for characterization of aquifer heterogeneities. Water Resour. Res. 38 (12), 60-1-60-15, http://dx.doi.org/10.1029/ 2001WR001176
- Böhm, G., Vesnaver, A., 1996. Relying on a grid. J. Seismic Explor. 5 (2), 169–184. Brauchler, R., Cheng, J.T., Dietrich, P., Everett, M., Johnson, B., Liedl, R., Sauter, M., 2007. An inversion strategy for hydraulic tomography: coupling travel time and amplitude inversion. J. Hydrol. 345 (3), 184–198, http://dx.doi.org/10. 1016/j.jhydrol.2007.08.011
- Brauchler, R., Hu, R., Dietrich, P., Sauter, M., 2011. A field assessment of high-resolution aquifer characterization based on hydraulic travel time and hydraulic attenuation tomography. Water Resour. Res. 47 (3), W03503, http://dx.doi.org/10.1029/2010WR009635
- Brauchler, R., Hu, R., Vogt, T., Al-Halbouni, D., Heinrichs, T., Ptak, T., Sauter, M., 2010. Cross-well slug interference tests: an effective characterization method for resolving aquifer heterogeneity. J. Hydrol. 345 (3), 184–198, http://dx.doi.org/10.1016/j.jhydrol.2010.01.004
- Brauchler, R., Liedl, R., Dietrich, P., 2003. A travel time based hydraulic tomographic approach. Water Resour. Res. 39 (12), 1370, http://dx.doi.org/10.1029/2003WR002262
- Brooks, R.H., Corey, T., 1964. Hydraulic properties of porous media. In: Hydrology Papers. Colorado State University (March).
- Burdine, N.T., 1953. Relative permeability calculations from pore size distribution data. J. Pet. Technol. 5, http://dx.doi.org/10.2118/225-G
- Butler, J.J., McElwee, C.D., Bohling, G.C., 1999. Pumping tests in networks of multilevel sampling wells: motivation and methodology. Water Resour. Res. 35 (11), 3553–3560.
- Chadwick, A., Arts, R., Eiken, O., Williamson, P., Williams, G., 2006. Geophysical monitoring of the CO₂ plume at Sleipner, North Sea. Adv. Geol. Storage Carbon Dioxide 65, 303–314.

- Chen, Z., Ewing, R.E., 1997. Fully discrete finite element analysis of multiphase flow in groundwater hydrology. SIAM J. Numer. Anal. 34 (6), 2228–2253.
- Cheng, J., Brauchler, R., Everett, M.E., 2009. Comparison of early and late travel times of pressure pulses induced by multilevel slug tests. Eng. Appl. Comput. Fluid Mech. 3 (4), 514–529.
- Daley, T.M., Freifeld, B.M., Ajo-Franklin, J., Dou, S., 2013. Field testing of fiber-optic distributed acoustic sensing (DAS) for subsurface seismic monitoring. Leading Edge 32 (6), 699–706, http://dx.doi.org/10.1190/tle32060699.1
- Dana, E., Skoczylas, F., 2002. Experimental study of two-phase flow in three sandstones. I. Measuring relative permeabilities during two-phase steady-state experiments. Int. J. Multiphase Flow 28 (11), 1719–1736, http://dx.doi.org/10.1016/S0301-9322(02)90-3
- Doherty, J., 2010. PEST: Model-Independent Parameter Estimation. Watermark Numerical Computing, Brisbane, Australia.
- Doughty, C., Freifeld, B.M., Trautz, R.C., 2008. Site characterization for CO₂ geologic storage and vice versa: the Frio brine pilot, Texas, USA as a case study. Environ. Geol. 54 (8), 1635–1656, http://dx.doi.org/10.1007/s00254-007-0942-0
- Doughty, C., Pruess, K., Benson, S.M., Gunter, W.D., 2004. Hydrological and geochemical monitoring for a CO₂ sequestration pilot in a brine formation. Lawrence Berkeley National Laboratory, LBNL-55104.
- Duan, Z., Hu, J., Li, D., Mao, S., 2008. Densities of the CO₂-H₂O and CO₂-H₂O-NaCl Systems up to 647 K and 100 MPa. Energy Fuels 22 (3), 1666–1674, http://dx.doi.org/10.1021/ef700666b
- Duan, Z., Sun, R., 2000. An improved model calculating CO₂ solubility in pure water and aqueous NaCl solutions from 273 to 533 K and from 0 to 2000. Chem. Geol. 193 (3), 257–271, http://dx.doi.org/10.1016/S0009-2541(02)263-2
- Finsterle, S., Pruess, K., 1996. Design and analysis of a well test for determining two-phase hydraulic properties. In: Report LBNL-39620. Lawrence Berkeley National Laboratory, Berkeley, California.
- Erlström, M., Rötting, T., Sperber, C., Shtivelman, V., Scadeanu, D., 2011. MUSTANG Deliverable D023, Report on property values and parameters, related uncertainties. Public report available at http://www.co2mustang.eu/.
- Fenghour, A., Wakeham, W.A., Vesovic, V., 1998. The viscosity of carbon dioxide. J. Phys. Chem. Ref. Data 27, 31, http://dx.doi.org/10.1063/1.556013
- Fokker, P.A., Borello, E.S., Serazio, C., Verga, F., 2012. Estimating reservoir heterogeneities from pulse testing. J. Petrol. Sci. Eng. 86, 15–26, http://dx.doi. org/10.1016/j.petrol.2012.03.017
- Fokker, P.A., Verga, F., 2011. Application of harmonic pulse testing to water-oil displacement. J. Petrol. Sci. Eng. 79 (3), 125–134, http://dx.doi.org/10.1016/j. petrol.2011.09.004
- Freyberg, D.L., 1986. A natural gradient experiment on solute transport in a sand aquifer: 2. Spatial moments and the advection and dispersion of nonreactive tracers. Water Resour. Res. 22 (13), 2031–2046.
- Gilbert, P., 1972. Iterative methods for the three-dimensional reconstruction of an object from projections. J. Theor. Biol. 36 (1), 105–117, http://dx.doi.org/10. 1016/0022-5193(72)90180-4
- Hammond, G.E., Lichtner, P.C., Mills, R.T., 2014. Evaluating the performance of parallel subsurface simulators: an illustrative example with PFLOTRAN. Water Resour. Res. 50 (1), 208–228, http://dx.doi.org/10.1002/2012WR013483
- Helmig, R., 1997. Multiphase Flow and Transport Processes in the Subsurface. Springer Berlin Heidelberg, Berlin, Heidelberg, http://dx.doi.org/10.1007/978-3-642-60763-9
- Hovorka, S.D., Doughty, C., Holtz, M., 2004. Testing efficiency of storage in the subsurface: Frio brine pilot experiment. Lawrence Berkeley National Laboratory. Retrieved from: http://escholarship.org/uc/item/8db8500>.
- Hu, R., Brauchler, R., Herold, M., Bayer, P., 2011. Hydraulic tomography analog outcrop study: Combining travel time and steady shape inversion. J. Hydrol. 409 (1) 350-362. http://dx.doi.org/10.1016/j.jibydrol.2011.08.031
- 409 (1), 350–362, http://dx.doi.org/10.1016/j.jhydrol.2011.08.031

 Illman, W.A., Craig, A.J., Liu, X., 2007. Practical issues in imaging hydraulic conductivity through hydraulic tomography. Ground Water 46 (1), 120–132, http://dx.doi.org/10.1111/j.1745-6584.2007.00374.x
- International Formulation Committee of the 6th International Conference on the Properties of Steam, 1967. The 1967 IFC Formulation for Industrial Use Verein Deutscher Ingenieure, Düsseldorf.
- IPCC, 2005. IPCC Special Report on Carbon Dioxide Capture and Storage. Prepared by Working Group Iii of the Intergovernmental Panel on Climate Change. In: Metz, B., Davidson, O., de Coninck, H.C., Loos, M., Meyer, L.A. (Eds.). Cambridge University Press, Cambridge.
- Jackson, M.J., Tweeton, D.R., 1996. 3DTOM: three-dimensional geophysical tomography. Report of Investigations 9617 US Department of the Interior, p. 84.
- Jiménez, S., Brauchler, R., Bayer, P., 2013. A new sequential procedure for hydraulic tomographic inversion. Adv. Water Resour. 62, 59–70, http://dx.doi.org/10. 1016/j.advwatres.2013.10.002
- Juanes, R., Spiteri, E.J., Orr, F.M., Blunt, M.J., 2006. Impact of relative permeability hysteresis on geological CO₂ storage. Water Resour. Res. 42 (12), http://dx.doi. org/10.1029/2005WR004806
- Krevor, S., Pini, R., Li, B., Benson, S.M., 2011. Capillary heterogeneity trapping of CO₂ in a sandstone rock at reservoir conditions. Geophys. Res. Lett. 38 (15), http://dx.doi.org/10.1029/2011GL048239
- Kulkarni, K.N., Datta-Gupta, A., Vasco, D.W., 2001. A streamline approach for integrating transient pressure data into high-resolution reservoir models. SPE J. 6 (3), 273–282, http://dx.doi.org/10.2118/74135-PA
- Lemieux, J., 2011. Review: the potential impact of underground geological storage of carbon dioxide in deep saline aquifers on shallow groundwater resources. Hydrogeol. J. 19 (4), 757–778, http://dx.doi.org/10.1007/s10040-011-0715-4

- Lichtner, P.C., 1996. Continuum formulation of multicomponent-multiphase reactive transport. Rev. Mineral. Geochem. 34, 1–81.
- Mao, D., Yeh, T.-C.J., Wan, L., Wen, J.-C., Lu, W., Lee, C.-H., Hsu, K.-C., 2013. Joint interpretation of sequential pumping tests in unconfined aquifers. Water Resour. Res. 49 (4), 1782–1796, http://dx.doi.org/10.1002/wrcr.20129
- Martinez-Landa, L., Rötting, T.S., Carrera, J., 2013. Use of hydraulic tests to identify the residual CO₂ saturation at a geological storage site. Int. J. Greenhouse Gas Control 19 (11), 652–664, http://dx.doi.org/10.1016/j.ijggc.2013.01.043
- Mishra, S., Kelley, M., Zeller, E., Slee, N., Gupta, N., Bhattacharya, I., Hammond, M., 2013. Maximizing the value of pressure monitoring data from CO₂ sequestration projects. Energy Procedia 37, 4155–4165, http://dx.doi.org/10.1016/j.egypro.2013.06.317
- Prats, M., Scott, J.B., 1975. Effect of wellbore storage on pulse-test pressure response. J. Petrol. Technol. 27 (06), 707–709, http://dx.doi.org/10.2118/5322-
- Robertson, E.C., 1988. Thermal properties of rocks. Open-file report 88-441, USGS. Rasmusson, K., Rasmusson, M., Fagerlund, F., Bensabat, J., Tsang, Y., Niemi, A., 2014. Analysis of alternative push-pull-test-designs for determining in situ residual trapping of carbon dioxide. Int. J. Greenhouse Gas Control 27, 155–168, http://dx.doi.org/10.1016/j.ijggc.2014.05.008
- Sminchak, J., Gupta, N., Gerst, J., 2009. Well test results and reservoir performance for a carbon dioxide injection test in the Bass Islands Dolomite in the Michigan Basin. Environ. Geosci. 16 (3), 153–162, http://dx.doi.org/10.1306/eg. 04080909001
- Somerton, W.H., El-Shaarani, A.H., Mobarak, S.M., 1974. High temperature behavior of rocks associated with geothermal type reservoirs. Paper SPE-4897. In: Proceedings of the 44th Annual California Regional Meeting of the Society of Petroleum Engineers, Richardson, TX: Society of Petroleum Engineers.
- Span, R., Wagner, W., 1996. A new equation of state for carbon dioxide covering the fluid region from the triple-point temperature to 1100 K at pressures up to 800 MPa. J. Phys. Chem. Ref. Data 25, 1509, http://dx.doi.org/10.1063/1.555991
- Sun, A.Y., Nicot, J.P., 2012. Inversion of pressure anomaly data for detecting leakage at geologic carbon sequestration sites. Adv. Water Resour. 44, 20–29, http://dx.doi.org/10.1016/j.advwatres.2012.04.006
- Vasco, D.W., Keers, H., Karasaki, K., 2000. Estimation of reservoir properties using transient pressure data: an asymptotic approach. Water Resour. Res. 36 (12), 3447–3465
- Vesnaver, A., Böhm, G., 2000. Staggered or adapted grids for seismic tomography? Leading Edge 19 (9), 944–950, http://dx.doi.org/10.1190/1.1438762
- Vilarrasa, V., Bolster, D., Dentz, M., Olivella, S., Carrera, J., 2010. Effects of CO₂ compressibility on CO₂ storage in deep saline aquifers. Transp. Porous Media 85 (2), 619–639. http://dx.doi.org/10.1007/s11242-010-9582-z
- 85 (2), 619–639, http://dx.doi.org/10.1007/s11242-010-9582-z
 Virieux, J., Flores-Luna, C., Gibert, D., 1994. Asymptotic theory for diffusive electromagnetic imaging. Geophys. J. Int. 119 (3), 857–868, http://dx.doi.org/10.1111/j.1365-246X.1994.tb04022.x
- Wang, C.Y., Beckermann, C., 1993. A two-phase mixture model of liquid-gas flow and heat transfer in capillary porous media-I. Formulation. Int. J. Heat Mass Transfer 36 (11), 2747–2758, http://dx.doi.org/10.1016/0017-9310(93)90094-
- Wiese, B., Böhner, J., Enachescu, C., Würdemann, H., 2010. Hydraulic characterisation of the Stuttgart formation at the pilot test site for CO₂ storage, Ketzin, Germany. Int. J. Greenhouse Gas Control 4 (6), 960–971, http://dx.doi.org/10.1016/j.ijggc.2010.06.013
- Wilke, C.R., Chang, P., 1955. Correlation of diffusion coefficients in dilute solutions. AIChE J. 1 (2), 264–270.
- Wu, C.-M., Yeh, T.-C.J., Zhu, J., Lee, T.H., Hsu, N.-S., Chen, C.-H., Sancho, A.F., 2005. Traditional analysis of aquifer tests: comparing apples to oranges? Water Resour. Res. 41 (9), W09402, http://dx.doi.org/10.1029/2004WR003717 Xiang, J., Yeh, T., Lee, C.H., Hsu, K.C., Wen, J.C., 2009. A simultaneous successive
- Xiang, J., Yeh, T., Lee, C.H., Hsu, K.C., Wen, J.C., 2009. A simultaneous successive linear estimator and a guide for hydraulic tomography analysis. Water Resour. Res. 45 (2), http://dx.doi.org/10.1029/2008WR007180
- Yeh, T., Liu, S., 2000. Hydraulic tomography: development of a new aquifer test method, Water Resour. Res. 36 (8), 2095–2105.
- Yeh, T., Zhu, J., 2007. Hydraulic/partitioning tracer tomography for characterization of dense nonaqueous phase liquid source zones. Water Resour. Res. 43 (6), W06435, http://dx.doi.org/10.1029/2006WR004877.